nature nanotechnology

LETTERS

https://doi.org/10.1038/s41565-018-0093-3

Experimental observation of chiral magnetic bobbers in B20-type FeGe

Fengshan Zheng[1], Filipp N. Rybakov[2,3,4], Aleksandr B. Borisov[3,4], Dongsheng Song[5], Shasha Wang[6,7], Zi-An Li[8], Haifeng Du[6,7]*, Nikolai S. Kiselev[9]*, Jan Caron[1], András Kovács[1], Mingliang Tian[6,7], Yuheng Zhang[6,7], Stefan Blügel[9] and Rafal E. Dunin-Borkowski[1]

Chiral magnetic skyrmions[1,2] are nanoscale vortex-like spin textures that form in the presence of an applied magnetic field in ferromagnets that support the Dzyaloshinskii–Moriya interaction (DMI) because of strong spin–orbit coupling and broken inversion symmetry of the crystal[3,4]. In sharp contrast to other systems[5,6] that allow for the formation of a variety of two-dimensional (2D) skyrmions, in chiral magnets the presence of the DMI commonly prevents the stability and coexistence of topological excitations of different types[7]. Recently, a new type of localized particle-like object—the chiral bobber (ChB)—was predicted theoretically in such materials[8]. However, its existence has not yet been verified experimentally. Here, we report the direct observation of ChBs in thin films of B20-type FeGe by means of quantitative off-axis electron holography (EH). We identify the part of the temperature–magnetic field phase diagram in which ChBs exist and distinguish two mechanisms for their nucleation. Furthermore, we show that ChBs are able to coexist with skyrmions over a wide range of parameters, which suggests their possible practical applications in novel magnetic solid-state memory devices, in which a stream of binary data bits can be encoded by a sequence of skyrmions and bobbers.

In non-centrosymmetric crystals with a strong spin–orbit interaction[9], such as B20-type MnSi (ref. [10]), FeGe (ref. [11]), $Fe_{1-x}Co_xSi$ (ref. [12]), $Mn_{1-x}Fe_xGe$ (ref. [13]), β-Mn-type Co–Zn–Mn alloys[14] and molybdenum nitrides[15], the competition between the ferromagnetic exchange interaction and the DMI results in a homochiral helical spin spiral ground state. The equilibrium period of such a spin spiral, $L_D = 4\pi A/D$, is governed by the ratio of the exchange stiffness A and the DMI constant D (ref. [16]). In a bulk sample, the spin spiral usually appears as a multidomain state, with a set of spiral $\mathbf{k}$-vector directions across domains[17]. In the presence of an external magnetic field, $\mathbf{B}_{ext}$, such a multidomain spiral state transforms into a monodomain conical state, with the magnetization $\mathbf{M}$ tilted towards the direction of $\mathbf{B}_{ext}$ and with $\mathbf{k} \parallel \mathbf{B}_{ext}$. The conical state persists as the lowest energy state over the entire range of applied magnetic fields up to a critical value of $B_D = D^2/2AM$, above which it converges to a saturated ferromagnetic state.

In a thin film of thickness $L \sim L_D$, the system undergoes a field-induced transition into a regular lattice of topologically non-trivial vortex-like spin textures—skyrmion tubes (SkTs) (Fig. 1a). Owing to the effect of a chiral surface twist, the energy of a skyrmion lattice becomes lower than that of the conical phase over a wide range of $\mathbf{B}_{ext}$ (ref. [18]). It has been shown both experimentally[11] and theoretically[18,19] that the range of magnetic fields for which skyrmions are the ground state depends on the film thickness, and above a threshold value the skyrmions become metastable. The mechanism for skyrmion stabilization in isotropic chiral magnets, including B20-type crystals with commonly weak cubic anisotropy, is different from that in ultrathin films and multilayers that possess strong out-of-plane magnetocrystalline anisotropy and in which the DMI appears due to a broken inversion symmetry at interfaces[20,21].

Although it has been assumed that the magnetic skyrmion is a unique localized spin texture in chiral magnets, it was recently predicted theoretically that, for film thicknesses that are larger than the equilibrium period $L \gtrsim L_D$ and magnetic fields $B_{ext} < B_D$, magnetic skyrmions may coexist with another type of localized particle-like object, the ChB[8,19] (Fig. 1a). The energy barriers that protect skyrmions and ChBs are of the same order of magnitude[8] and the two objects are potentially ideal candidates for use as '1' and '0' bit carriers (Fig. 1b). The potential advantages of using such an approach for binary data encoding[22], when compared to the recently proposed skyrmion-based racetrack memory[23], are discussed in detail in Supplementary Section 1.

Here, we report the experimental observation of ChBs in thin plates of B20-type FeGe by means of off-axis EH. EH provides quantitative measurement of the phase shift φ of the incident electron beam in a transmission electron microscope (TEM) with a high spatial resolution. The phase shift originates from the interaction of the electrons with the projected in-plane component of the magnetic induction within and around the sample[24]. As a ChB has a finite penetration depth and occupies a much smaller volume of the sample than a SkT, the phase shift at the position of a ChB is expected to be significantly weaker than that at a SkT (Fig.1c–e). A quantitative comparison between the experimentally measured and theoretically calculated phase-shift difference $\Delta\varphi$, which is defined in Fig. 1e, allows ChBs and SkTs to be identified and distinguished unambiguously.

Owing to the interaction of localized objects, the shapes of SkT and ChB can be slightly distorted and the penetration depth of

[1]Ernst Ruska-Centre for Microscopy and Spectroscopy with Electrons and Peter Grünberg Institute, Forschungszentrum Jülich, Jülich, Germany. [2]Department of Physics, KTH-Royal Institute of Technology, Stockholm, Sweden. [3]M.N. Miheev Institute of Metal Physics of Ural Branch of Russian Academy of Sciences, Ekaterinburg, Russia. [4]Ural Federal University, Ekaterinburg, Russia. [5]National Center for Electron Microscopy in Beijing, School of Materials Science and Engineering, Tsinghua University, Beijing, China. [6]The Anhui Key Laboratory of Condensed Matter Physics at Extreme Conditions, High Magnetic Field Laboratory and University of Science and Technology of China, Chinese Academy of Science (CAS), Hefei, Anhui Province, China. [7]Collaborative Innovation Center of Advanced Microstructures, Nanjing University, Jiangsu Province, China. [8]Institute of Physics, Chinese Academy of Sciences, Beijing, China. [9]Peter Grünberg Institute and Institute for Advanced Simulation, Forschungszentrum Jülich and JARA, Jülich, Germany. *e-mail: duhf@hmfl.ac.cn; n.kiselev@fz-juelich.de

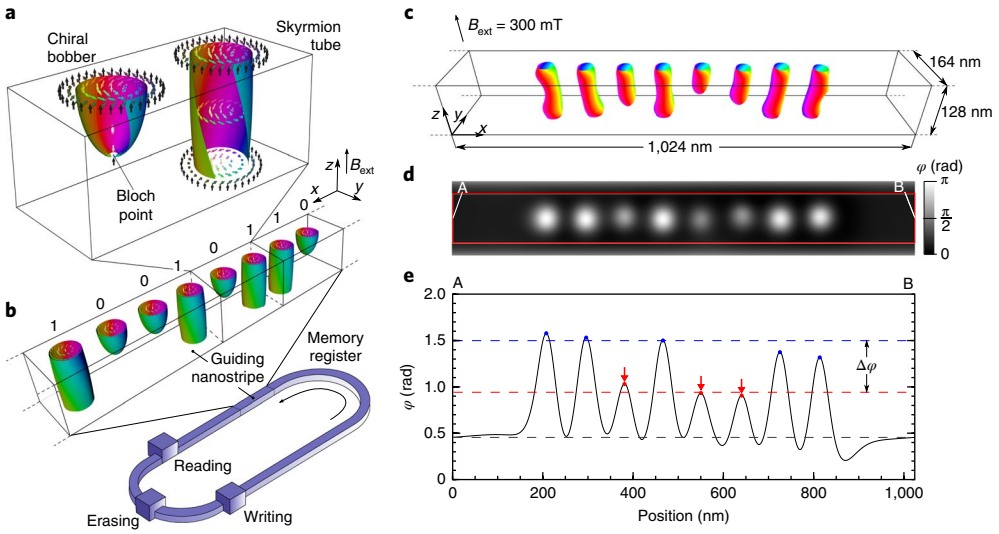

Fig. 1 | ChBs and SkTs in a nanostripe. a, Schematic representation of spin structures for a magnetic ChB and a SkT, which are represented by isosurfaces defined by the positions of the spins oriented perpendicular to the *z* axis. Here and below, the colours of the vectors and the isosurfaces are defined by the in-plane component of the magnetization, according to a standard colour wheel (Supplementary Fig. 7). **b**, New concept for magnetic solid-state memory based on encoding a data stream in a nanostripe, which takes the form of a closed track that contains a chain of alternating magnetic SkTs and ChBs that correspond to 1 and 0 bits. The actions of writing, reading and erasing units are performed at different positions along the guiding track. **c**, Results of micromagnetic simulations performed for a chain of SkTs and ChBs in an FeGe nanostripe in the presence of an external magnetic field applied along $\mathbf{e}_z$. The 3D vector field of equilibrium magnetization obtained after full relaxation is represented by isosurfaces that correspond to those in **a**. **d**, Phase shift of an electron beam φ calculated for the magnetization distribution shown in **c**. **e**, Profile of the phase-shift map in **d** averaged over the width of the band marked by the red rectangle. The blue, red and black dashed lines in **e** correspond to the average signal of a SkT, a ChB and the nearly homogeneous state in between them, respectively. The red arrows indicate peaks that correspond to ChBs. $\Delta\varphi$ is the difference in height between peaks that correspond to SkTs and those that correspond to ChBs.

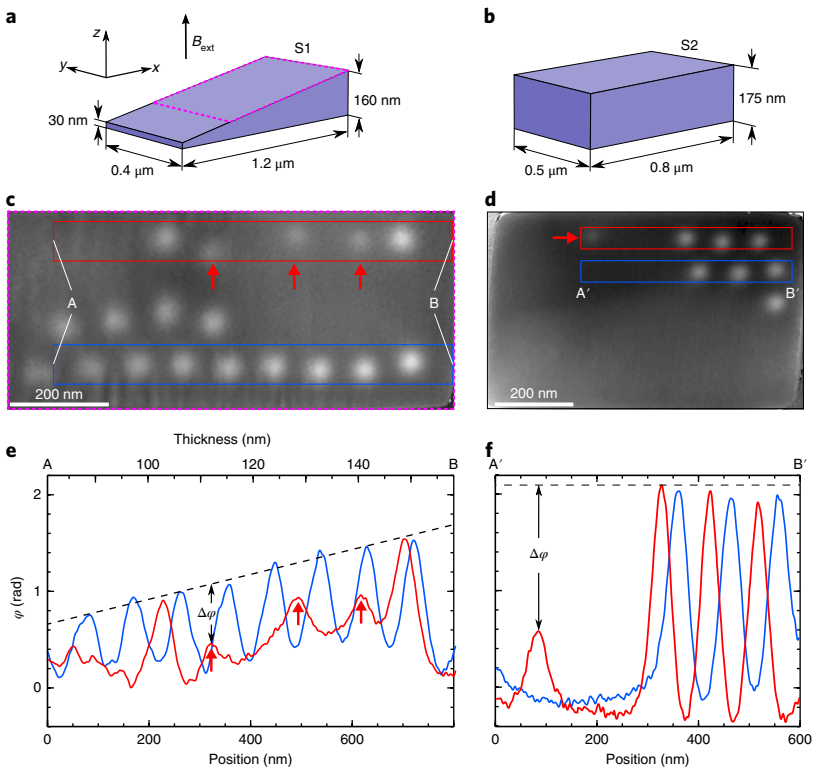

Fig. 2 | Experimental evidence for the nucleation of chiral magnetic bobbers by means of in-field cooling. a,**b**, Sizes and geometries of a wedge-shaped (**a**) and rectangular (**b**) FeGe stripes. **c**,**d**, Magnetic-phase-shift images that correspond to **a** and **b**, respectively, recorded in the presence of a 300 mT magnetic field after in-field cooling. Image **c** corresponds to the dotted magenta rectangle in **a**. The red arrows indicate objects with weak contrast that are identified as ChBs. **e**,**f**, Phase-shift profiles as a function of position that correspond to the bands of the same colour marked in **c** and **d**, respectively. The dashed line in **e**, which represents a trend line for the phase shifts of SkTs, exhibits a nearly linear increase due to the gradient in specimen thickness.

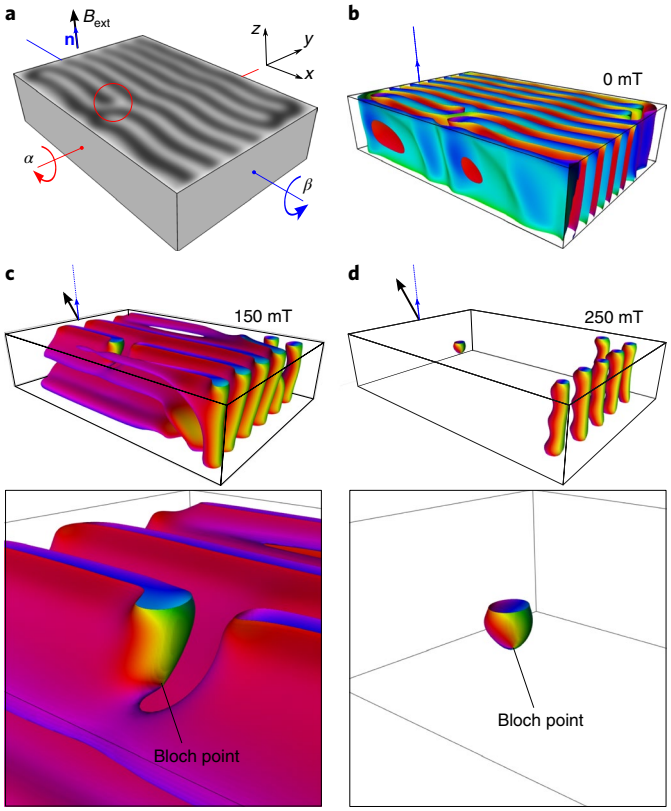

Fig. 3 | Nucleation of a ChB from an edge dislocation in the helical state in an inclined external magnetic field. a, Schematic representation of a sample and two orthogonal axes of rotation α and β. The vector **n** is normal to the plane of the sample. **b**, Initial configuration of a helical state represented by corresponding isosurfaces, as in Fig. 1c. A corresponding phase-shift map is shown on the top surface of the cuboid in **a**, with the position of an edge dislocation marked by a red circle. **c**, Nucleation of a Bloch point at $B_{ext}=150$ mT tilted by $\beta=5°$. **d**, ChB at $B_{ext}=250$ mT with $\beta=5°$. The images below **c** and **d** are magnified views of the corresponding images. The size of the simulated domain is $540\times800\times180$ nm^3. The isosurfaces in **c** and **d** are defined in Fig. 1a–c.

ChB may deviate from the equilibrium value that corresponds to the case of isolated ChB in a pure conical phase. Hence, the maximum of the phase shift that corresponds to a particular SkT and ChB may slightly deviate from the values averaged over the different configurations (horizontal dashed lines in Fig. 1e). Such deviations are typically very weak and provide significant contributions to the absolute values of the phase-shift peaks only at relatively low fields when both SkTs and ChBs become highly distorted.

We chose thin plates of B20-type FeGe to demonstrate the formation of ChBs. FeGe is well known for its near-room-temperature magnetic transition, $T_c\approx278$ K, and for the relatively small period of its helical spin spiral, $L_D\approx70$ nm. A magnetic field applied perpendicular to an FeGe plate typically induces a transition to a skyrmion lattice at higher temperatures or individual SkTs at a lower temperatures[11]. Most of our EH measurements were carried out on three samples: S1, a nanostripe with varying thickness (Fig. 2a); S2, a rectangular-shaped sample of fixed thickness (Fig. 2b) and S3, a plate with a large lateral size and a nearly fixed thickness (Supplementary Table 1). Representative EH data discussed in the main text were obtained primarily from sample S2. The other samples are described in Supplementary Figs. 2–5.

Based on a theoretical prediction of the spontaneous nucleation of ChBs during in-field cooling[8], we performed a series of EH experiments by cooling the samples at a fixed value of $\mathbf{B}_{ext}\parallel\mathbf{e}_z$. Representative magnetic-phase-shift images and the corresponding line profiles recorded from samples S1 and S2 after cooling from temperature $T_{max}=240$ K to $T=95$ K at $B_{ext}=200$ mT and then increasing B_{ext} to 300 mT are shown in Fig. 2c–f. For both samples, the phase-shift images show contrast that is typical for magnetic skyrmions in the form of bright spots of nearly identical intensity and size with bell-like profiles (Fig. 2c,d). A phase-shift image recorded from a wedge-shaped sample is characterized by a linear increase in phase shift associated with a thickness gradient dashed trend line in Fig. 2e, in agreement with a previous experiment[25]. Significantly, a quantitative analysis of the phase-shift profiles reveals the presence of two distinct types of objects, which are characterized by different phase shifts and large values of $\Delta\varphi$. The objects with weaker contrast, which are marked in Fig. 2c,d by red arrows, show a close similarity to the emergence of ChBs in micromagnetic simulations (Fig. 1c–e). Such weaker-intensity features appeared in the wedge-shaped sample only above a certain value of film thickness ($L\gtrsim110\,\text{nm}\approx1.6L_D$). These objects exhibit a magnetic-field dependence of their position, size and intensity (Supplementary Fig. 2). As all of these properties are consistent with theoretical predictions, the weaker intensity objects are identified as ChBs. Although their formation is reproducible, the nucleation of each ChB corresponds to a metastable state in the presence of in-field cooling and is a rare event. In most cases, a change of T_{max} and B_{ext} from their optimal values of 240 K and 200 mT, respectively, results in the formation of a pure multi-skyrmion state (Supplementary Fig. 3).

To perform a systematic study of ChBs, we established a more-reliable approach for their nucleation on the basis of micromagnetic simulations, which predicted the nucleation of ChBs from edge-dislocation defects in helical spin spirals in the presence of a tilted applied magnetic field (Fig. 3). With increasing field strength, the isosurfaces of a helical spin spiral reflect the tilt of the **k**-vector of the spiral towards the direction of $\mathbf{B}_{ext}$. At a certain value of B_{ext}, the tilt leads to the formation of a fold in the isosurface, which in turn gives rise to the formation of a Bloch point that penetrates from the surface to a certain depth into the volume of the sample (Fig. 3c). This state only remains stable over a narrow range of B_{ext} and transforms to a complete ChB on further increasing the field (Fig. 3d). A similar mechanism is responsible for the emergence of Bloch points in a skyrmion lattice and a helical magnetic state[26,27]. As edge dislocations and similar defects occur often in the helical state, the process of demagnetization commonly leads to the formation of Bloch points and to the nucleation of ChBs in an inclined magnetic field.

In our experimental set-up, the direction of the applied magnetic field is fixed and coincides with the direction of the incident electron beam. A tilt of the field is then achieved by rotating the sample about two mutually orthogonal axes α and β, such that $\mathbf{B}_{ext}$ makes an angle of ~10° to the plate normal **n**. At such a tilt angle, a small number of magnetization–demagnetization cycles is sufficient to nucleate ChBs. After the nucleation of ChBs, the sample was returned to a zero tilt angle and measurements of the phase shift were performed using EH. Representative phase-shift images of ChBs in sample S2 obtained using this approach are shown in Fig. 4a–g. Corresponding images recorded from samples S1 and S3 are shown in Supplementary Figs. 4 and 5.

The images clearly illustrate: (1) the reproducibility of ChB nucleation in an inclined magnetic field, (2) the appearance of ChBs in different positions in the sample, (3) the mobility of ChBs in an applied magnetic field and (4) quantitative agreement between experimentally measured phase-shift values and the theoretical calculations. Figure 4h shows the theoretical phase shift calculated based on the results of micromagnetic simulations for the configuration that corresponds to a pair of SkTs and a single ChB, similar to that in the experimental image shown in Fig. 4d. The comparison between the experimental and theoretical phase-shift profiles across three

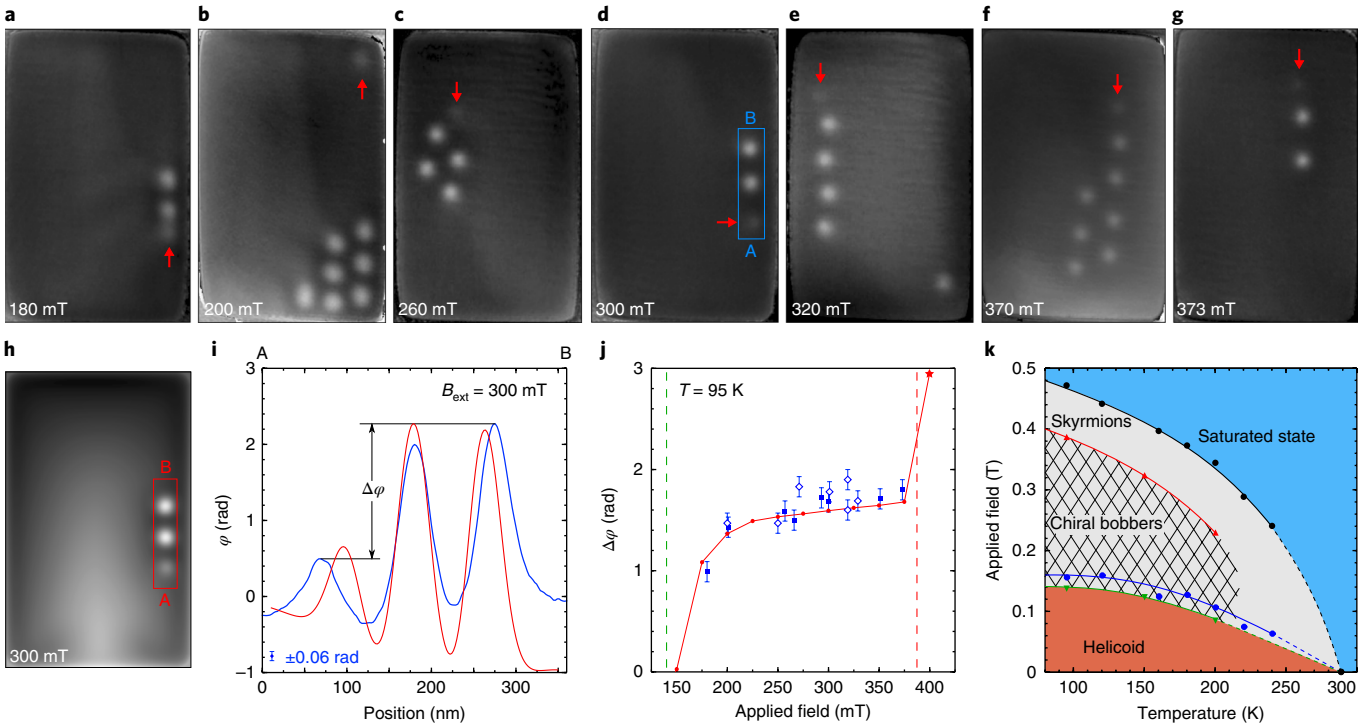

Fig. 4 | Stability of chiral magnetic bobbers in different fields and temperatures. a–g, Phase-shift images of magnetic skyrmions and ChBs examined in increasing fields from left to right. The images shown in **a**,**d**,**g** were obtained during the course of a single experiment, whereas the others were recorded during separate experiments, which illustrates the reproducibility of the effect. All of the images were recorded at a temperature of 95 K. The positions of ChBs are marked by red arrows. **h**, Theoretical magnetic phase shift calculated from micromagnetic simulations (Supplementary Figs. 6 and 7). The two brighter spots correspond to SkTs, whereas the weaker spot corresponds to a ChB. **i**, Phase-shift profiles along the bands indicated in **d** and **h** measured from rectangles with the corresponding colours. The red and blue plots correspond to the theoretical and experimental images, respectively. The magnitude of the error in the experimental measurements, which results from instabilities in the microscope and biprism and from the detector characteristics, is indicated in the lower left corner. **j**, Phase differences, $\Delta\varphi$, between signals from SkTs and ChBs recorded at $T = 95$ K for various configurations and plotted as a function of the applied magnetic field. The circles connected by a red line represent theoretical dependence of $\Delta\varphi$ calculated for the configuration with one ChB and two SkTs (**h** and Supplementary Figs. 7 and 8). Blue solid squares correspond to the experimental dataset similar to the theoretically calculated configuration (**a**,**d**,**g** and Supplementary Fig. 6). The open diamonds correspond to other configurations with a large number of SkTs, such as in **b**,**c**,**e**,**f**. The error bar in **j** represents the systematic error that originates from experimental measurements of the phase shift. The vertical dashed lines are the ranges of the existence of ChBs determined experimentally at $T = 95$ K. The green line corresponds to an elliptical instability, whereas the red line corresponds to ChB collapse. The star represents a sharp increase in the theoretical phase shift due to the abrupt shrinkage of a ChB in a high magnetic field. **k**, Magnetic phase diagram that shows the experimentally measured range of existence of SkTs (grey) and ChBs (hatched) in sample S2 of 175 nm thickness. The blue line marks the nucleation field for skyrmions in an increasing field. The green lines correspond to an elliptical instability for both SkTs and ChBs. The red and black lines correspond to the collapse fields for ChBs and SkTs, respectively. As a result of thermal fluctuations for $T \geq 200$ K, a reliable estimation of the critical fields for ChBs was precluded. Above $T = 240$ K, all of the transition lines are extrapolated to zero at $T_c = 278$ K. Further details about the phase diagram are available in Supplementary Section 2.

bright spots (Fig. 4i) shows an excellent quantitative agreement of the relative differences between the phase shifts of SkTs and ChB, $\Delta\varphi$. The predicted magnetic field dependence of $\Delta\varphi$ is fully consistent with the experimental data (Fig. 4j and Supplementary Figs. 6–8). Small deviations of the experimentally measured values of $\Delta\varphi$ from the theoretical trend line of approximately ± 0.2 rad may result from: (1) a slight surface roughness after the focused ion beam (FIB) sample preparation, (2) the presence of electrostatic charges on the sample surface and (3) small variations of $\Delta\varphi$ that depend on the adjacent physical and magnetic texture of the sample.

Our simulations predict the abrupt shrinkage of ChBs between 375 mT and 400 mT (Supplementary Figs. 7 and 8). Such small ChBs remain stable in the simulations, but collapse rapidly in the presence of very small perturbations, such as those produced by only a 2° tilt of B_{ext}. This transition, which corresponds to a collapsed field, agrees well with the experimentally measured value of 387 mT (red dashed line in Fig. 4j).

Both the equilibrium distance between a ChB and the edge of the sample and the SkT–edge distance increase with increasing applied magnetic field, which suggests the same character of interaction. The distances between the ChBs and SkTs observed at 320 mT (Fig. 4e) and 370 mT (Fig. 4f) are approximately the same as the intersky-rmion distance, which confirms the presence of interactions that define the equilibrium distances between ChBs and SkTs, which are similar to the Lennard–Jones-type interactions for SkTs[28].

Our implementation of a reliable method for ChB nucleation also allowed us to study the stability of ChBs at elevated temperatures. Figure 4k shows a magnetic phase diagram constructed from an extensive set of measurements made over a wide range of temperatures and applied magnetic fields (Supplementary Figs. 9–11). The grey region corresponds to the range of stability of magnetic skyrmions and is bounded by a collapse field (black line) and an elliptical instability field (green line). The blue line corresponds to SkT nucleation, that is, to the transition with increasing applied magnetic field from a helical spin spiral to isolated skyrmions. The elliptical instability field has a lower value than the field for SkT nucleation, which gives rise to a weak hysteresis.

The hatched area inside the grey region corresponds to the range of existence of ChBs and is bounded from the bottom by the same elliptical instability field as for the SkTs, but has a much lower collapse field than that for SkTs. Above 200 K, it is no longer possible to distinguish reliably between SkTs and ChBs because of thermal fluctuation and spontaneous drift.

In summary, our work provides the direct observation of theoretically predicted particle-like objects, ChBs, that coexist together with magnetic skyrmions in thin films of cubic chiral magnets. These objects represent a promising area of further fundamental research and possible practical applications. In particular, the presence of two types of localized movable object suggests an alternative approach for data encoding, in which a data stream can be encoded in a single chain composed of two distinct particles.

Note added in proof: During the review process, we became aware of a submitted paper that reports on a new stable magnetic phase in an epitaxial film of FeGe/Si(111) (ref. [29]). The results of magnetization measurements presented in the paper are interpreted as evidence of the formation of a layer of ChBs at the FeGe/Si interface.

Methods

Methods, including statements of data availability and any associated accession codes and references, are available at https://doi.org/10.1038/s41565-018-0093-3.

Received: 8 May 2017; Accepted: 14 February 2018;
Published online: 9 April 2018

References

1. Bogdanov, A. N. & Yablonskii, D. A. Thermodynamically stable 'vortices' in magnetically ordered crystals. The mixed state of magnets. *Sov. Phys. JETP* **68**, 101 (1989).
2. Ivanov, B. A., Stephanovich, V. A. & Zhmudskii, A. A. Magnetic vortices—the microscopic analogs of magnetic bubbles. *J. Magn. Magn. Mater.* **88**, 116 (1990).
3. Dzyaloshinskii, I. A thermodynamic theory of 'weak' ferromagnetism of antiferromagnetics. *J. Phys. Chem. Solids* **4**, 241–255 (1958).
4. Moriya, T. Anisotropic superexchange interaction and weak ferromagnetism. *Phys. Rev.* **120**, 91–98 (1960).
5. Belavin, A. A. & Polyakov, A. M. Metastable states of two-dimensional isotropic ferromagnets. *JETP Lett.* **22**, 245 (1975).
6. Piette, B. M. A. G., Schroers, B. J. & Zakrzewski, W. J. Multisolitons in a two-dimensional Skyrme model. *Z. Phys. C.* **65**, 165–174 (1995).
7. Koshibae, W. & Nagaosa, N. Theory of antiskyrmions in magnets. *Nat. Commun.* **7**, 10542 (2016).
8. Rybakov, F. N., Borisov, A. B., Blügel, S. & Kiselev, N. S. New type of particlelike state in chiral magnets. *Phys. Rev. Lett.* **115**, 117201 (2015).
9. Kanazawa, N., Seki, S. & Tokura, Y. Noncentrosymmetric magnets hosting magnetic skyrmions. *Adv. Mater.* **29**, 1603227 (2017).
10. Yu, X. et al. Variation of skyrmion forms and their stability in MnSi thin plates. *Phys. Rev. B* **91**, 054411 (2015).
11. Yu, X. Z. et al. Near room-temperature formation of a skyrmion crystal in thin-films of the helimagnet FeGe. *Nat. Mater.* **10**, 106–109 (2011).
12. Yu, X. Z. et al. Real space observation of a two-dimensional skyrmion crystal. *Nature* **465**, 901–904 (2010).
13. Shibata, K. et al. Towards control of the size and helicity of skyrmions in helimagnetic alloys by spin–orbit coupling. *Nat. Nanotech.* **8**, 723–728 (2013).
14. Tokunaga, Y. et al. A new class of chiral materials hosting magnetic skyrmions beyond room temperature. *Nat. Commun.* **6**, 7638 (2015).
15. Li, W. et al. Emergence of skyrmions from rich parent phases in the molybdenum nitrides. *Phys. Rev. B* **93**, 060409 (2016).
16. Dzyaloshinskii, I. E. Theory of helicoidal structures in antiferromagnets. III. *Sov. Phys. JETP* **20**, 665 (1965).
17. Lebech, B., Bernhard, J. & Freltoft, T. Magnetic structures of cubic FeGe studied by small-angle neutron scattering. *J. Phys. Condens. Matter* **35**, 6105 (1989).
18. Rybakov, F. N., Borisov, A. B. & Bogdanov, A. N. Three-dimensional skyrmion states in thin films of cubic helimagnets. *Phys. Rev. B* **87**, 094424 (2013).
19. Rybakov, F. N., Borisov, A. B., Blügel, S. & Kiselev, N. S. New spiral states and skyrmion lattice in 3D model of chiral magnet. *New. J. Phys.* **18**, 045002 (2016).
20. Romming, N., Kubetzka, A., Hanneken, C., von Bergmann, K. & Wiesendanger, R. Field-dependent size and shape of single magnetic skyrmions. *Phys. Rev. Lett.* **114**, 177203 (2015).
21. Boulle, O. et al. Room-temperature chiral magnetic skyrmions in ultrathin magnetic nanostructures. *Nat. Nanotech.* **11**, 449–454 (2016).
22. Kiselev, N. S., Bogdanov, A. N., Schäfer, R. & Rößler, U. K. Chiral skyrmions in thin magnetic films: new objects for magnetic storage technologies? *J. Phys. D.* **44**, 392001 (2011).
23. Fert, A., Cros, V. & Sampaio, J. Skyrmions on the track. *Nat. Nanotech.* **8**, 152–156 (2013).
24. Midgley, P. A. & Dunin-Borkowski, R. E. Electron tomography and holography in materials science. *Nat. Mater.* **4**, 271–280 (2009).
25. Park, H. S. et al. Observation of the magnetic flux and three-dimensional structure of skyrmion lattices by electron holography. *Nat. Nanotech.* **9**, 337–342 (2014).
26. Milde, P. et al. Unwinding of a skyrmion lattice by magnetic monopoles. *Science* **340**, 1076–1080 (2013).
27. Schütte, C. & Rosch, A. Dynamics and energetics of emergent magnetic monopoles in chiral magnets. *Phys. Rev. B* **90**, 174432 (2014).
28. Leonov, A. O., Monchesky, T. L., Loudon, J. C. & Bogdanov, A. N. Three-dimensional chiral skyrmions with attractive interparticle interactions. *J. Phys. Condens. Matter* **28**, 35 (2016).
29. Ahmed, A. S. et al. Chiral bobber formation in epitaxial FeGe/Si(111) films. Preprint at http://arXiv.org/abs/1706.08248v1 (2017).

Acknowledgements

This work was supported by the National Key R&D Program of China, grant no. 2017YFA0303201, the Natural Science Foundation of China, grant nos 51622105 and 11474290, the Key Research Program of Frontier Sciences, CAS, grant no. QYZDB-SSW-SLH009, the Key Research Program of the Chinese Academy of Science, grant no. KJZD-SW-M01, the Major/Innovative Program of Development Foundation of Hefei Center for Physical Science and Technology, grant no. 2016FXCX001 and the Youth Innovation Promotion Association CAS no. 2015267. F.Z. and R.E.D.-B. acknowledge the European Union for funding through the Marie Curie Initial Training Network SIMDALEE2. The research leading to these results has received funding from the European Research Council under the European Union's Seventh Framework Programmer (FP7/2007–2013)/ERC grant agreement no. 320832. The work of F.N.R. was supported by the Swedish Research Council grant no. 642-2013-7837. The work of A.B.B. was carried out within the state assignment of FASO of Russia (theme Quantum no. 01201463332).

Author contributions

N.S.K. and H.D. contributed to the planning of this study. F.N.R. proposed the concept and, together with A.B.B., performed the preliminary simulations. F.Z. together with D.S., S.W., N.S.K. and H.D. performed the experiments. H.D., A.K. and R.E.D.-B. supervised and designed the experiments. N.S.K. performed the micromagnetic simulations and prepared the initial version of the manuscript. J.C. calculated the theoretical phase-shift images. F.N.R., M.T., S.B. and R.E.D.-B. edited the manuscript. All of the authors discussed the results and contributed to the preparation of the manuscript.

Competing interests

The authors declare no competing interests.

Additional information

Supplementary information is available for this paper at https://doi.org/10.1038/s41565-018-0093-3.

Reprints and permissions information is available at www.nature.com/reprints.

Correspondence and requests for materials should be addressed to H.D. or N.S.K.

Publisher's note: Springer Nature remains neutral with regard to jurisdictional claims in published maps and institutional affiliations.

Methods

Sample preparation. Specimens were prepared from a polycrystal of B20-type FeGe using a FIB workstation and a lift-out method[30,31].

Off-axis EH. Off-axis electron holograms were recorded using an electrostatic biprism positioned in a conjugated image plane in an FEI Titan 60–300 TEM operated at 300 kV. The microscope was operated in the aberration-corrected Lorentz mode with the sample in magnetic-field-free conditions. A conventional microscope objective lens was used to apply the chosen vertical (out-of-plane) magnetic fields of between −0.15 and 1.5 T, which were precalibrated using a Hall probe. A liquid-nitrogen-cooled specimen holder (Gatan model 636) was used to vary the sample temperature between 95 and 380 K. Lorentz images and off-axis electron holograms were recorded both using a 2k × 2k charge-coupled device camera (Gatan Ultrascan), Fig. 2c and Supplementary Figs. 1–3, and using a direct electron counting K2-IS camera[32] (Gatan). A total of 20 object electron holograms and 20 vacuum reference electron holograms, each with a 6 s exposure time, were usually recorded to improve the signal-to-noise ratio in the phase images[33,34]. The hologram interference fringe contrast was typically 50%. The standard deviation of the phase values measured in a vacuum region adjacent to the sample was in the range 0.04–0.06 rad. The off-axis electron holograms were analysed using a standard fast Fourier transform algorithm in Holoworks software (Gatan).

Magnetic imaging in the TEM. Magnetic imaging in the TEM was performed in the Lorentz mode with the objective lens of the microscope turned off to provide magnetic-field-free conditions at the position of the sample. In the Fresnel mode of Lorentz TEM, the intensity distribution at defocus Δz is recorded to reveal a bright or dark contrast at the positions of the magnetic domain walls. Large defocus values of several tens or hundreds of micrometres are typically required. For a Bloch-type magnetic skyrmion, the presence of a rotating magnetic field results in an intensity maximum or minimum in a defocused image, depending on its helicity and on the sign of the defocus. The technique is straightforward to implement and provides a direct qualitative image that reveals the positions at which the projected in-plane magnetization in the sample changes abruptly. However, it is difficult to extract quantitative information from such images or to study magnetic structures that are a few tens of nanometres in size or smaller.

The TEM mode of off-axis EH[24,35] is based on the interference of an object wave of primary interest with a tilted plane reference wave. The resulting interference fringe pattern is modulated locally in contrast and position by the amplitude and phase of the object wave. The intensity distribution in the interference pattern can be written in the form:

$$I(x,y) = A_1^2 + A_2^2 + 2A_1A_2\cos(\Delta\phi) \quad (1)$$

where A_i is the amplitude of each wave and $\Delta\phi$ is the phase difference between them at each point across the field of view.

In a quantum mechanical description, an incident electron wave experiences a phase shift on travelling through an electromagnetic potential that can be expressed in the form:

$$\varphi(x,y) = \varphi_E + \varphi_M = C_E \int V\,dz - \frac{2\pi e}{h}\int A_z\,dz \quad (2)$$

where the incident electron-beam direction z is perpendicular to the xy plane, C_E is an interaction constant that takes a value of 6.53×10^6 rad V^{-1} m^{-1} at an accelerating voltage of 300 kV, V is the electrostatic potential, e is the elementary charge of an electron 1.6×10^{-19} C, h is Planck's constant 6.63×10^{-34} m^2 kg s^{-1} and A_z is the component of the magnetic vector potential along z. The magnetic vector potential $\mathbf{A}$ is related to the magnetic flux density by the expression $\mathbf{B} = \nabla\times\mathbf{A}$. In the absence of long-range charge redistribution within and around the sample and electron-beam-induced specimen charging, V comprises primarily the mean inner potential (MIP) of the material V_0, which depends on its composition, density and ionicity. The magnetic contribution to the phase shift that results from an enclosed magnetic flux, Φ_M (without the necessity for classical interaction with a $\mathbf{B}$ field) is described by the Aharonov–Bohm effect. The magnetic contribution to the recorded phase shift between two arbitrary points in a phase image can be written in the form:

$$\varphi_M = -\frac{2\pi e}{h}\oint \mathbf{A}\,d\mathbf{l} \quad (3)$$

for a rectangular loop ($\mathbf{l}$) that is formed by two parallel electron trajectories crossing the sample and joined, at infinity, by segments perpendicular to their trajectories. With reference to equation (3), Stokes' law can be used to show that:

$$\varphi_M = -2\pi\frac{e}{h}\Phi_M S \quad (4)$$

where $h/e = 4.135\times10^{-15}$ T m^2 is a flux quantum (the magnetic flux that results in a phase difference of 2π) and S is the area of the loop that encloses the magnetic flux. Supplementary Fig. 1 shows the sequence of experimental and data-processing steps that is required to obtain a magnetic phase map of B20-type FeGe skyrmions and bobbers. Off-axis electron holograms were first recorded from the sample and from a vacuum reference area (not shown) using the same illumination conditions, as shown in Supplementary Fig. 1a. Inset I of Supplementary Fig. 1a shows a magnified region of interference fringes, which are slightly bent as a result of local variations in the in-plane magnetic field at the positions of the skyrmions. A Fourier transform of the hologram of the sample, which is shown in inset II of Supplementary Fig. 1a, contains a centre band and two sidebands, as well as streaks that are associated with Fresnel fringes from the edges of the biprism wire. The local variation in intensity around the sidebands results from phase shifts introduced by the sample. Reconstruction of the holograms involves digitally selecting one of the sidebands using an aperture (inset II Supplementary Fig. 1a), followed by centring it in Fourier space and calculating its inverse Fourier transform. The phase of the resulting complex image $\phi = \arctan(i/r)$ is evaluated from the imaginary i and real r parts of the wavefunction, whereas the amplitude is obtained from the expression $a = \sqrt{r^2+i^2}$. The difference between the object phase and the phase of the vacuum reference hologram (Supplementary Fig. 1b) is initially evaluated modulo 2π and therefore contains phase discontinuities, which can be 'unwrapped' using suitable algorithms (Supplementary Fig. 1c). To separate the magnetic contribution to the phase shift from the MIP contribution, phase images were recorded from the B20-type FeGe sample both at low temperature (Supplementary Fig. 1c) and at room temperature (Supplementary Fig. 1d). The two phase images were then aligned and subtracted from each other (on the assumption that the MIP is the same and that there are no changes in diffraction contrast or specimen charging, contamination or damage between the two temperatures). Supplementary Fig. 1e shows the final magnetic contribution to the phase shift of the skyrmion lattice in B20-type FeGe, which can be evaluated quantitatively.

The present EH measurements do not allow a reconstruction of the 3D magnetic configuration within and around the sample and only provide information about the in-plane magnetic induction projected in the direction of the incident electron beam. As a result, it is not possible to determine whether the ChBs are located at the top or the bottom surface of the sample, or whether they form a coupled state, with two ChBs located at both surfaces, as predicted theoretically[8].

Micromagnetic simulations. Initial micromagnetic simulations for a simplified model without dipole–dipole interactions were performed using software described previously[8] and the phenomenon of merging of SkTs and ChBs into chains or clusters was found. The final micromagnetic simulations were performed using MuMax[36] using the energy functional:

$$\begin{aligned} E &= \int_{V_s}\{E_{ex} + E_{DMI} + E_Z + E_d\}\,d\mathbf{r} \\ E_{ex} &= A\,(\partial_x\mathbf{m}^2 + \partial_y\mathbf{m}^2 + \partial_z\mathbf{m}^2) \\ E_{DMI} &= D\mathbf{m}[\nabla\times\mathbf{m}] \\ E_Z &= -M_s\mathbf{B}_{ext}\mathbf{m},\ E_d = -\frac{1}{2}M_s\mathbf{B}_d\mathbf{m} \end{aligned} \quad (5)$$

where $\mathbf{m}\equiv\mathbf{m}(x,y,z)$ is a unit continuous vector field ($|\mathbf{m}|=1$) that represents the magnetization $M = M_s\mathbf{m}$, A and D are the micromagnetic constants for exchange and DMI, respectively, M_s is the saturation magnetization of the material, $\mathbf{B}_{ext}$ is the applied magnetic field and $\mathbf{B}_d$ is the demagnetizing field generated by the divergence of the magnetization within the volume of the sample and at its edges. As a result of the relatively high magnetic moment of $\mu_{Fe}\approx1\mu_B$, the stray fields, which depend on the shape and size of the sample, make a significant contribution to the total magnetic energy[37]. The integration in equation (5) extends over the entire volume of the sample, V_s. In our calculations, we assume the material parameters $M_s = 384$ kA m^{-1}, $A = 4.75$ pJ m^{-1} and $D = 0.853$ mJ m^{-2}, defined from the expression for the equilibrium period of the spin spiral $L_D = 4\pi A/D$, for which the typical value in FeGe is 70 nm. The mesh size of the simulated domain was $528\times82\times64$ cells. Each cell was a cube of edge length 2 nm. To achieve a state with alternating skyrmions and ChBs, as shown in Fig. 1c, we initiated the simulations from a homogeneously magnetized state, either with SkTs that penetrated the entire thickness of the nanostripe or with tubes that ended in the mid-plane of the sample. After energy minimization using a conjugate-gradient method, the spin structure was exported to the Spirit code (https://spirit-code.github.io) for the advanced visualization of isosurfaces.

The presence of Bloch point magnetic singularities does not lead to a divergence in the total energy[38]. The dynamics and equilibrium configurations of the system can still be calculated using a micromagnetic approach, as has been shown for permalloy disks[39] and thin films[40].

Calculation of magnetic phase images. The calculation of magnetic phase images from a 3D magnetization distribution is based on the Aharonov–Bohm equation. The magnetic vector potential $\mathbf{A}(\mathbf{r})$ can be expressed in terms of the magnetization $\mathbf{M}(\mathbf{r})$ by using the convolution integral[41]:

$$\mathbf{A}(\mathbf{r}) = \frac{\mu_0}{4\pi} \int_{V_S} \mathbf{M}(\mathbf{r}') \times \frac{\mathbf{r}-\mathbf{r}'}{|\mathbf{r}-\mathbf{r}'|^3} \mathrm{d}\mathbf{r}' \quad (6)$$

where integration is performed over the volume of the magnetic material. The combination of the magnetic parts of equations (2) and (6) yields an equation that directly links the magnetization distribution to the magnetic contribution to the phase shift in the form:

$$\varphi_M = -\mu_0 \frac{e}{h} \int \frac{(y-y')\mathrm{M}_x(x',y') - (x-x')\mathrm{M}_y(x',y')}{(x-x')^2 + (y-y')^2} \mathrm{d}x'\mathrm{d}y' \quad (7)$$

where $\mathrm{M}_{x,y}$ are the projections of the in-plane magnetization distribution[42]:

$$\mathrm{M}_x(x',y') = \int M_x(\mathbf{r}')\mathrm{d}z', \ \mathrm{M}_y(x',y') = \int M_y(\mathbf{r}')\mathrm{d}z' \quad (8)$$

and integration is performed over the thickness of the magnetic material along the line defined as $x=x'$ and $y=y'$.

In the discretized form, projection and convolution can be executed in two separate steps, both of which can be described in terms of a matrix operation that leads to the equation:

$$\mathbf{y} = QP\mathbf{x} \quad (9)$$

where P is the projection matrix, Q is the convolution matrix, $\mathbf{x}$ is the magnetic state vector (that is, M in vectorized form) and the vector $\mathbf{y}$ contains the vectorized form of the calculated magnetic phase image. An efficient implementation of the projection step can be achieved by employing sparse matrix calculations, especially in the case of the projection along the z axis. To optimize the second step, the convolution kernels (equation (7)) were precalculated by using known analytical solutions for simple magnetized geometries in real space and by employing fast convolutions in Fourier space.

Data availability. The data that support the plots within this paper and other findings of this study are available from the corresponding authors on reasonable request.

References

30. Du, H. et al. Edge-mediated skyrmion chain and its collective dynamics in a confined geometry. *Nat. Commun.* **6**, 8504 (2015).
31. Jin, C. et al. Control of morphology and formation of highly geometrically confined magnetic skyrmions. *Nat. Commun.* **8**, 15569 (2017).
32. Chang, S. L. Y., Dwyer, C., Barthel, J., Boothroyd, C. B. & Dunin-Borkowski, R. E. Performance of a direct detection camera for off-axis electron holography. *Ultramicroscopy* **161**, 90–97 (2016).
33. Voelkl, E. & Tang, D. Approaching routine 2π/1000 phase resolution for off-axis electron holography. *Ultramicroscopy* **110**, 447–459 (2010).
34. McLeod, R. A., Bergen, M. & Malac, M. Phase measurement error in summation of electron holography series. *Ultramicroscopy* **141**, 38–50 (2014).
35. Lichte, H. & Lehmann, M. Electron holography—basics and applications. *Rep. Prog. Phys.* **71**, 016102 (2008).
36. Vansteenkiste, A. et al. The design and verification of MuMax3. *AIP Adv.* **4**, 107133 (2014).
37. Shibata, K. et al. Temperature and magnetic field dependence of the internal and lattice structures of skyrmions by off-axis electron holography. *Phys. Rev. Lett.* **118**, 087202 (2017).
38. Döring, W. Point singularities in micromagnetism. *J. Appl. Phys.* **39**, 1006 (1968).
39. Thiaville, A., Garca, J. M., Dittrich, R., Miltat, J. & Schrefl, T. Micromagnetic study of Bloch-point-mediated vortex core reversal. *Phys. Rev. B* **67**, 094410 (2003).
40. Zverev, V. V. & Filippov, B. N. Simulation of three-dimensional micromagnetic structures in magnetically uniaxial films with in-plane anisotropy: static structures. *Phys. Met. Metallogr.* **114**, 108–115 (2013).
41. Mansuripur, M. Computation of electron diffraction patterns in Lorentz electron microscopy of thin magnetic films. *J. Appl. Phys.* **69**, 2455–2464 (1991).
42. Kovács, A. et al. Mapping the magnetization fine structure of a lattice of Bloch-type skyrmions in an FeGe thin film. *Appl. Phys. Lett.* **111**, 192410 (2017).